Review on exsolution and its driving forces in perovskites

IOP Publishing J. Phys. Energy 2 (2020) 032001 https://doi.org/10.1088/2515-7655/ab8c1f

Journal of Physics: Energy

OPEN ACCESS

RECEIVED
8 January 2020

REVISED
1 April 2020

ACCEPTED FOR PUBLICATION
22 April 2020

PUBLISHED
27 May 2020

TOPICAL REVIEW

Review on exsolution and its driving forces in perovskites

Ohhun Kwon[1,4], **Sangwook Joo**[1,4], **Sihyuk Choi**[2,5], **Sivaprakash Sengodan**[3,5] **and Guntae Kim**[1,5]

[1] Department of Energy Engineering, Ulsan National Institute of Science and Technology (UNIST), Ulsan 44919, Republic of Korea
[2] Department of Mechanical Engineering, Kumoh National Institute of Technology, Gyeongbuk 39177, Republic of Korea
[3] Department of Materials, Imperial College London, London SW7 2AZ, United Kingdom
[4] These authors contributed equally to this work.
[5] Authors to whom any correspondence should be addressed.

E-mail: sh.choi@kumoh.ac.kr, s.sengodan@imperial.ac.uk **and** gtkim@unist.ac.kr

Keywords: exsolution, perovskite, driving force, catalysis

Abstract

Exsolution is a promising method to design metal nanoparticles for electrocatalysis and renewable energy. Metal nanoparticles exsolved from perovskite oxide lattices have been utilized as catalysts in many energy fields because of their high durability and excellent electro-catalytic properties. Although this method has received much attention in recent years, a comprehensive understanding is still lacking because of difficulties in finding a rational combination of driving forces and perovskite supports. Thus, the aim of our work here is to recapitulate the principles of exsolution and collect various exsolution studies by categorizing the driving forces of exsolution and the structural characteristics of perovskite supports. These classifications provide guidelines for selecting suitable materials groups and remodeling existing materials, thereby exploring applications of catalysts using exsolution that are applicable to academic and industrial fields.

1. Introduction

Metal nanoparticles, active sites of electrochemical reactions, have been intensively researched toward the development of more stable and effective catalysts due to their key role in electrochemical energy devices, electronics, optics, and catalysis [1–4]. Since metal nanoparticles are difficult to keep secure and stable, heterogeneous composites that introduce a supporting material to immobilize high-surface-area catalytic particles have been developed. Such composite materials are fabricated by depositing metal nanoparticles on the surface of the supporting material through chemical vapor deposition (CVD) or infiltration methods [5–7]. However, the deposited metal nanoparticles may undergo agglomeration and coarsening during cell operating conditions, leading to fatal performance degradation. Thus, an exsolution technique has been received extensive attention as a promising alternative.

Exsolution is a phenomenon in which metal catalysts are segregated from an oxide lattice to an oxide surface under a reducing atmosphere [8, 9]. Unlike the conventional deposition techniques, exsolution is particularly attractive for its time efficiency because no additional process is required for catalyst addition. Additionally, the exsolved metal nanoparticles have the unique feature of socketing into the oxide surface (figure 1(a)), enhancing cohesion between the metal nanoparticles and the supporting material [10]. Consequently, well-distributed and stable catalysts can be formed on the supporting material surface through the exsolution. The two key factors in producing nanocatalysts through exsolution are: (1) the perovskite supports should have high redox stability and (2) the metal cations should easily come to the surface under a reducing atmosphere. However, the complicated relationship between these factors and the numerous combinations with various perovskite oxides make the phenomena difficult to understand. Therefore, it is essential to identify and organize the exsolution phenomena to choose a rational catalyst.

This review begins with an overview of the general characteristics and driving forces of exsolution in perovskite oxides. Although several articles reviewing the exsolution have been published previously [12, 13], intensive research of exsolution is a recent endeavor, thus it is necessary to recapitulate the principles of the phenomena, and to collect scattered studies. Therefore, we intend to provide guidelines for selecting suitable

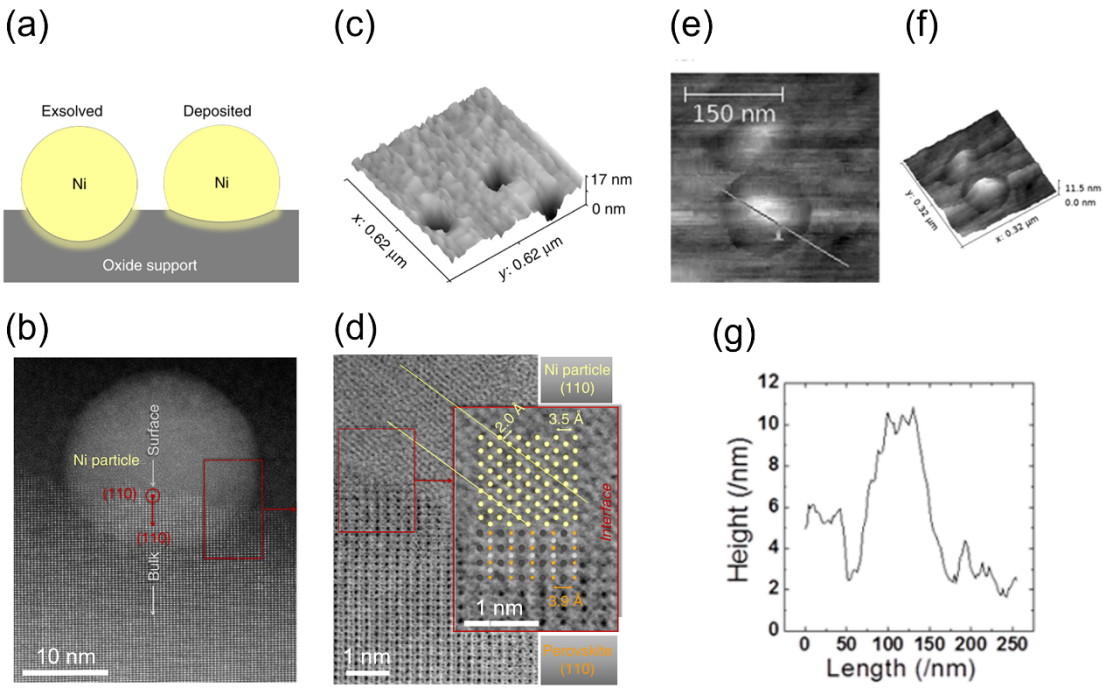

Figure 1. (a) Schematic illustration of the particle-substrate interface for deposited and exsolved nickel particles. (b) TEM micrograph (dark field) of a Ni particle exsolved on (110) native surface facet (see figure 1(d)) after ageing (~3% H_2O/5% H_2/Ar, 930 °C, 60 h). (c) Three-dimensional AFM of sockets. (d) TEM image detail (bright field) of the corresponding atomic planes and orientations. (e) AFM image after reduction at 700 °C (15 min, dry H_2). (f) 3D view of figure 1(e). (g) AFM height profile along the line shown in figure 1(e). (a), (b), (c), and (d) Reproduced with permission from [10], Copyright 2015, Nature Publishing Group. (e), (f), and (g) Reproduced with permission from [11], Copyright 2015 American Chemical Society.

groups of materials based on a fundamental understanding of exsolution, thereby exploring catalyst applications using exsolution that are applicable to both academic and industrial fields.

2. Characteristics and driving forces of exsolution in perovskite oxides

In this section, we introduce the general characteristics of nanocatalysts produced by exsolution. The general characteristics include morphology, carbon deposition characteristics, reversibility, and exsolution mechanism. Several studies highlight a morphological study of particle-substrate interactions with anchored nanoparticles [10]. As shown in transmission electron microscopy (TEM) analysis (figures 1(b) and (d)), the exsolved Ni particles have a pinned structure that is approximately 30% submerged into the parent oxide. Additionally, the atomic force microscopy (AFM) view of the etched surface (figure 1(c)) demonstrated that nanoparticles were embedded in the oxide matrix to a significant depth. Detailed exsolution morphology is described in a study by Oh *et al* [11]. As described by this study, exsolution proceeds through the formation of subsurface nucleates, and the movement of metal nucleate to the surface is accompanied by the formation of a pit on the surface where the particle emerges (figures 1(e)–(g)). Socketed structural features resulted in improved thermal stability of the catalyst and significantly reduced coke formation. This can be attributed to carbon fiber growth in exsolved particles occurring as a base-growth, unlike typical carbon fiber that undergoes tip-growth (figure 2(a)). In this case, the base growth of carbon fiber is restrained compared to the tip growth of carbon fiber.

Dopant cations dissolved in the parent oxide lattice matrix are released and then anchored to the surface under a reducing atmosphere, and this process is said to have redox reversibility if it can occur in reverse. It has been speculated that particles generally re-dissolve back into the perovskite oxide under an oxidizing atmosphere. However, as reported by Neagu *et al* [14], Ni and Co-Ni particles do not re-dissolve back into the underlying perovskite host lattice during the oxidation in $La_{0.8}Ce_{0.1}Ni_{0.4}Ti_{0.6}O_3$ and $La_{0.7}Ce_{0.1}Co_{0.3}Ni_{0.1}Ti_{0.6}O_3$ systems (figure 3). In the Co-Ni system, approximately 0.06 exsolved B-site atoms per unit cell, which is thought to make re-dissolution less favorable with the larger amount of 0.2 preferred for A-site vacancy.

The exsolution mechanism has been actively studied in recent years. Exsolution is a chemically driven heterogeneous phase transition, and Gao *et al* [15] proposed that exsolution arises from the four physical processes of diffusion, reduction, nucleation, and growth (figure 4(a)). Exsolving dopant cations are first

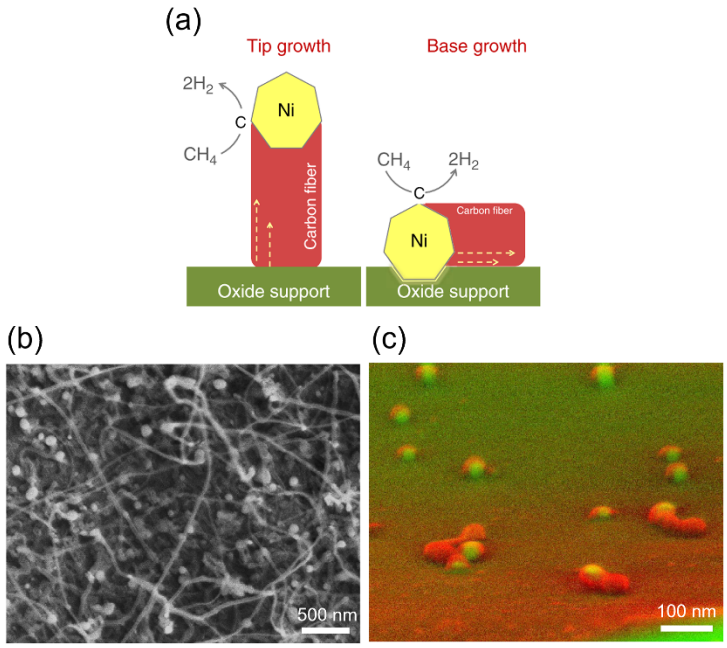

Figure 2. (a) Schematic of possible carbon fiber growth mechanisms. (b) Ni particles (30–100 nm) prepared by vapor deposition on $La_{0.4}Sr_{0.4}TiO_3$ showing considerable carbon fiber growth. (c) False color micrograph depicting a side view detail of $La_{0.52}$ $Sr_{0.28}Ni_{0.06}Ti_{0.94}O_3$ (5% H_2, 880 °C, 6 h). Reprinted with permission. (a), (b), and (c) Reproduced with permission from [10] Copyright 2015, Nature Publishing Group.

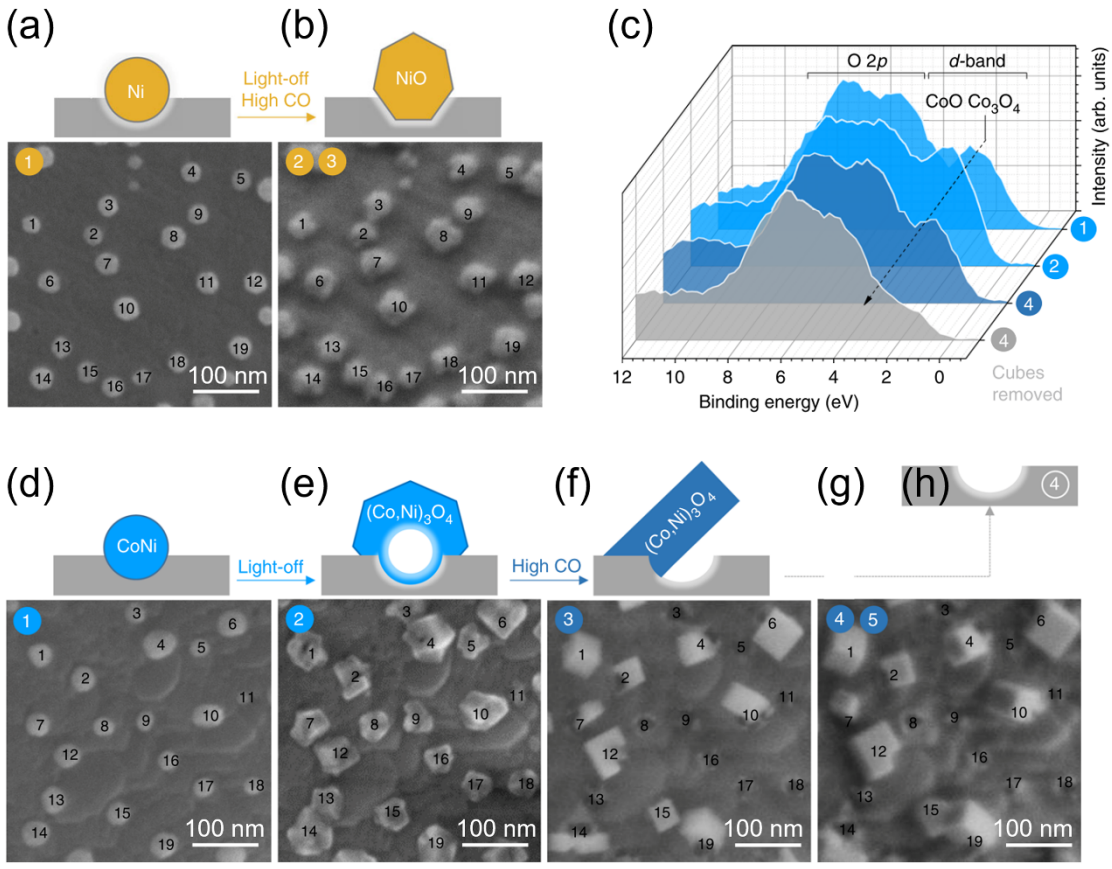

Figure 3. (a)–(b), (d)–(g) SEM images of tracked areas collected at room temperature at highlighted stages of catalytic testing, and corresponding cross-section schematics of the particle-perovskite interface. (c) XPS valence band spectra, guideline showing evolution of Co_3O_4 phase across selected samples. (h) Schematic of the local appearance of the perovskite surface after cube removal. Reproduced with permission from [14] Copyright 2017, Nature Publishing Group.

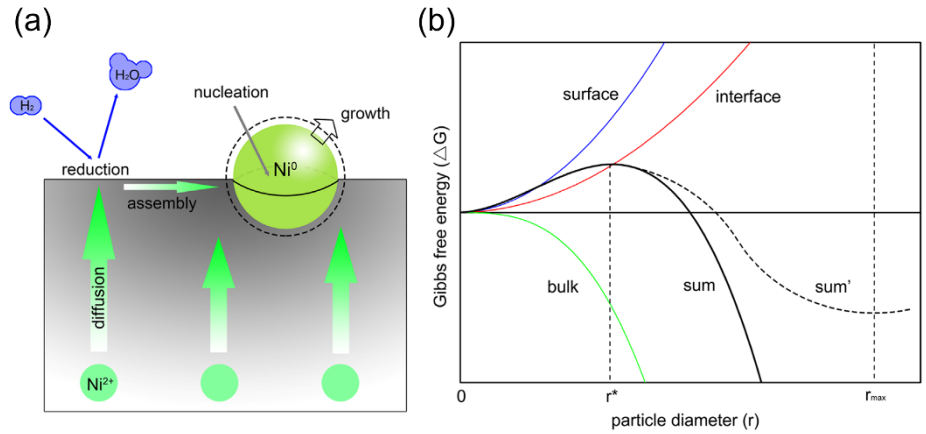

Figure 4. (a) Illustration of the exsolution process. (b) Gibbs free energy change during the nucleation and growth. Reprinted with permission. (a) and (b) Reproduced with permission from [15] Copyright 2016, Elsevier.

diffused from the bulk to the surface and then reduced to metal. Reduced metals are assembled into small nanoparticles that grow in size over the treatment time. Recently, direct observation of particle nucleation and growth during the exsolution has confirmed that the particles grow epitaxially and isotropically while maintaining their original positions [16]. The study also demonstrated that exsolution is limited by the exsolvable ion availability rather than diffusion to the surface. Gao *et al* [15] studied the effect of reducing time and atmosphere composition on particle growth and proposed three analytical models for growth, in which particle growth can be limited by strain, reactant amount, and diffusion. The results suggest that both the size-related strain and limited amounts of Ni could be possible mechanisms determining the particle size growth rate. However, the actual exsolution mechanism is likely a much more complex process than the models suggest, as nucleation, growth, and particle interaction need to be considered simultaneously.

Since the exsolution occurs under a reducing atmosphere, a general driving force of exsolution is an oxygen vacancy formation in the perovskite oxides. The oxygen vacancy formation destabilizes the lattice stoichiometry, causing the segregation of B-site cations to maintain structural stability. Several driving forces, such as temperature, non-stoichiometry by A-site defect, voltage biasing, strain, phase transition, and topotactic ion exchange, have been introduced to form the oxygen vacancy (figure 5). However, the degree of oxygen vacancy formation differs for each perovskite structure. Thus, the following sections discuss various exsolution phenomena and structural properties in the perovskite oxides to develop a more detailed understanding. A list of materials by structure and driving force is given in table 1.

2.1. Exsolution on stoichiometric single perovskite

Perovskite oxides (ABO_3) and derived structures (e.g. double perovskite ($A_2B_2O_{5+\delta}$) and Ruddlesden–Popper (RP, $A_{n+1}B_nO_{3\,n+1}$))-based materials have been mainly studied as the support materials for exsolution due to their excellent structural and compositional flexibility (figure 6). In typical perovskite oxides, it is possible to withstand some lattice mismatch between A–O and B–O bonds, thus allowing doping with different types of cations at each site [60, 61]. This flexibility of the perovskite structure enables the combination of a wide range of constituent ions, providing a variety of catalytic properties. In particular, studies have been conducted on redox couples such as $Ti^{3+/4+}$, $Mn^{3+/4+}$, $Ce^{3+/4+}$, $Mo^{4+/6+}$, $Cr^{3+/4+}$, $Nb^{4+/5+}$, and $V^{3+/4+/5+}$, which can be stable under a redox atmosphere.

Early exsolution concepts were applied to stoichiometric perovskite with A/B = 1, in which only readily reducible cations (e.g. Ni^{2+}, Ru^{2+}, Rh^{4+}, Pd^{4+}, and Pt^{4+}) could be exsolved to metal nanoparticles [62]. In such a case, most cations remain in the bulk, thus the number of nanoparticles available on the surface is limited. Since $LaFe_{0.57}Co_{0.38}Pd_{0.05}O_3$ [9] opened the possibility of *in situ* growth catalysts, perovskite oxides (ABO_3) have been employed as supporting frameworks. In early research, noble metals (e.g. Pd [9, 63], Ru [19, 20, 64], Rh, and Pt) were doped into B-site in perovskite lattice and partly exsolved under a reducing atmosphere. The Pd-perovskite catalyst [9] lasted about 100 h in an aging test under an atmosphere consisting of engine exhaust. The mol percentage of Pd was increased to 0.2 in $La_{0.8}Sr_{0.2}Cr_{0.8}Pd_{0.2}O_{3-\delta}$ [17], and the elimination of Pd nanoparticles upon oxidation and their re-nucleation upon reduction were observed. Meanwhile, Hamada *et al* [65] proposed a possible mechanism for the self-regeneration of Pd catalysts in $LaFe_{1-x}Pd_xO_3$. On the basis of the density functional theory (DFT) calculations, oxygen vacancies stabilized the surface segregation of Pd in the perovskite supporting material, forming $LaPdO_{3-y}$ in the

Table 1. Representative materials for exsolution in the various perovskites and driving forces.

Classification	Catalysts	Nature of materials	Environmental conditions for exsolution	Catalytic applications	Stability (hrs)
Stoichiometric single perovskite	$LaFe_{0.57}Co_{0.38}Pd_{0.05}O_3$ [9]	Noble metal in B-site		Autumotive emissions control	100
	$LaFe_{0.95}Pd_{0.05}O_3$ [9]	Noble metal in B-site		Autumotive emissions control	100
	$La_{0.8}Sr_{0.2}Cr_{0.8}Pd_{0.2}O_{3-\delta}$ [17]	Noble metal in B-site		SOFC anode	-
	$La_{0.8}Sr_{0.2}Fe_{0.9}Nb_{0.1}Pd_{0.04}O_{3-\delta}$ [18]	Noble metal in B-site		SOFC anode	100
	$La_{0.8}Sr_{0.2}Cr_{1-y}X_yO_{3-\delta}$ (X = Ni, Ru) [19]	Noble metal in B-site		SOFC anode	~100
	$La_{0.8}Sr_{0.2}Cr_{0.82}Ru_{0.18}O_{3-\delta}$ [19]	Noble metal in B-site		SOFC anode	50
	$La_{0.8}Sr_{0.2}Cr_{1-x}Ru_xO_{3-\delta}$ [20]	Noble metal in B-site		SOFC anode	60
	$LaCr_{0.95}Ir_{0.05}O_{3-\delta}$ [21]	Noble metal in B-site		Reforming catalysts	72
	$La_{1-x}Sr_xCr_{1-y}Ni_yO_{3-\delta}$ [22]	Ni metal in B-site	Temperature and gas condition	Reforming catalysts	-
	$La_{0.5}Sr_{0.5}Ti_{0.75}Ni_{0.25}O_{3-\delta}$ [23]	Ni metal in B-site		SOC electrode	-
	$(La_{0.7}Sr_{0.3})(Cr_{0.85}Ni_{0.1125}Fe_{0.0375})O_{3-\delta}$ [24]	Ni-Fe metal in B-site		SOFC anode	-
	$(La_{0.3}Sr_{0.6}Ce_{0.1})Ni_{0.1}Ti_{0.9}O_{3-\delta}$ [25]	Ni metal in B-site		SOFC anode	60
	$La_{0.75}Sr_{0.25}Cr_{0.5}Mn_{0.3}Ni_{0.2}O_{2.8}$ [26]	Ni metal in B-site		SOFC anode	-
	$La_{0.6}Sr_{0.4}Fe_{0.8}Ni_{0.2}O_{3-\delta}$ [27]	Ni-Fe metal in B-site		Carbon dioxide electrolyzer	100
	$(La_{0.75})(Sr_{0.25})(Cr_{0.5}Fe_{0.35}Ni_{0.15})O_3$ [28]	Ni-Fe metal in B-site		Reforming catalyst	20
	$Sr_2Fe_{1.4}Ni_{0.1}Mo_{0.5}O_{6-\delta}$ [29]	Ni metal in B-site		SOC electrode	-
	$La_{0.3}Sr_{0.7}Cr_{0.3}Fe_{0.6}Co_{0.1}O_{3-\delta}$ [30]	Co-Fe metal in B-site		-	-
	$La_{0.52}$ $Sr_{0.28}Ti_{0.94}Ni_{0.06}O_3$ [10]		Temperature and gas condition	Reforming catalysts	~80
	$La_{0.2}$ $Sr_{0.7}Ni_{0.1}Ti_{0.9}O_{3-\delta}$ [31]		Temperature and gas condition		
	$La_{0.4}Sr_{0.4}M_x{}^{n+}Ti_{1-x}O_{3-\delta}$ [32] (M = Fe^{3+} or Ni^{2+})		SOEC cathode condition	SOEC cathode	
	$La_{0.43}Ca_{0.37}Ni_{0.06}Ti_{0.94}O_{3-\delta}$ [33]		SOEC cathode condition	SOC electrode	150
	$La_{0.43}Ca_{0.37}Ni_{0.03}Fe_{0.03}Ti_{0.94}O_{3-\delta}$ [34]		SOEC cathode condition	Carbon dioxide electrolyzer	-
	$(La_{0.2}Sr_{0.8})_{0.95}Ti_{0.85}Mn_{0.1}Ni_{0.05}O_3$ [35]		SOEC cathode condition	Carbon dioxide electrolyzer	100
	$(La_{0.3}Sr_{0.7})_{0.9}Ti_{0.95}Ni_{0.05}O_{3-\delta}$ [36]		SOEC cathode condition	Carbon dioxide electrolyzer	~50
Non-stoichiometric single perovskite	$La_{0.4}Sr_{0.4}Sc_{0.9}Ni_{0.1}O_{3-\delta}$ [15]	A-site deficiency	Temperature and gas condition	SOFC anode	-
	$La_{0.9}Mn_{0.8}Ni_{0.2}O_3$ [37]		Temperature and gas condition	Reforming catalyst	24
	$La_{0.6}Sr_{0.3}Cr_{0.85}Ni_{0.15}O_{3-\delta}$ [38]		Temperature and gas condition	SOFC anode	-
	$(La_{0.3}Sr_{0.7})_{0.9}Ti_{0.9}Ni_{0.1}O_{3-\delta}$ [39]		Temperature and gas condition	SOEC cathode	-
	$(La_{0.2}Sr_{0.8})_{0.9}(Ti_{0.9}Mn_{0.1})_{0.9}Ni_{0.1}O_{3-\delta}$ [40]		Temperature and gas condition	Carbon dioxide electrolyzer	-
	$La_{0.4}Sr_{0.4}Ti_{0.9}Ni_{0.1}O3_{-\delta}$ [41]		Temperature and gas condition	HER catalyst in basic media	-
	$(La_{0.75}Sr_{0.25})_{0.9}(Cr_{0.5}Mn_{0.5})_{0.9}Cu_{0.1}O_{3-\delta}$ [42]		Temperature and gas condition	Carbon dioxide electrolyzer	
	$(La_{0.2}Sr_{0.8})_{0.9}Ti_{0.9}Cu_{0.1}O_{3-\delta}$ [43]		Temperature and gas condition	SOEC cathode	24
	$Sr_{0.95}Ag_{0.05}Nb_{0.1}Co_{0.9}O_{3-\delta}$ [44]		Temperature and gas condition	SOFC cathode	140
	$(La_{0.8}Sr_{0.2})_{0.95}Ag_{0.05}MnO3_{-\delta}$ [45]		Temperature and gas condition	DSSC cathode	-
	$Sr_{0.95}Ti_{0.3}Fe_{0.63}Ni_{0.07}O_{3-\delta}$ [46]		Temperature and gas condition	SOFC anode	-

Table 1. Continued.

Classification	Catalysts	Nature of materials	Environmental conditions for exsolution	Catalytic applications	Stability (hrs)
Double perovskite	$PrBaMn_2O_{5+\delta}$ [47]	Phase transition	Temperature and gas condition	SOFC anode	
	$PrBaMn_{1.7}Co_{0.3}O_{5+\delta}$ [47]	Phase transition		SOFC anode	
	$PrBaMn_{1.7}Ni_{0.3}O_{5+\delta}$ [47]	Phase transition		SOFC anode	200
	$PrBaMn_{1.7}Fe_{0.3}O_{5+\delta}$ [47]	Phase transition		SOFC anode	
	$NdBaMn_2O_{5+\delta}$ [48]	Phase transition		SOFC anode	
	$PrBaMn_{1.7}Co_{0.1}Ni_{0.2}O_{5+\delta}$ [49]	Phase transition		SOFC anode and Reforming catalyst	500
	$PrBaMn_{1.7}Co_{0.3}O_{5+\delta}$—Fe infiltration [50]	Phase transition and topotactic exchange		SOFC anode and Reforming catalyst	200
	$PrBaMn_{1.8}Co_{0.2}O_{5+\delta}$ [51]	Phase transition		SOFC anode and SOEC cathode	
	(Pr0.4Sr0.6)3(Fe0.85Nb0.15)2O7 [52]	Phase transition		SOFC anode	100
	$Sr_3FeMoO_{7-\delta}$ [53]	Phase transition		SOFC anode	24
	$Pr_{0.8}Sr_{1.2}(Co,Fe)_{0.8}Nb_{0.2}O_{4+\delta}$ [54]	Phase transition		SOFC anode	500
RP perovskite	$La_{1.2}Sr_{0.8}Mn_{0.4}Fe_{0.6}O_4$ [55]	Phase transition	Temperature and gas condition	SOFC anode	
	$Sr_3FeMoO_{6.5}$ [56]	Phase transition		SOFC anode	
	$La_{0.8}Sr_{1.2}Fe_{0.9}Co_{0.1}O_{4-\delta}$ [57]	K_2NiF_4-type structural perovskite		Symmetrical SOFC electrode	
	$La_{1.2}Sr_{0.8}Co_{0.4}Mn_{0.6}O_4$ [58]	Phase transition		CO_2 electrolysis	
	$SrGdNi_{0.2}Mn_{0.8}O_{4\pm\delta}$ [59]	K_2NiF_4-type structural perovskite		SOFC anode	

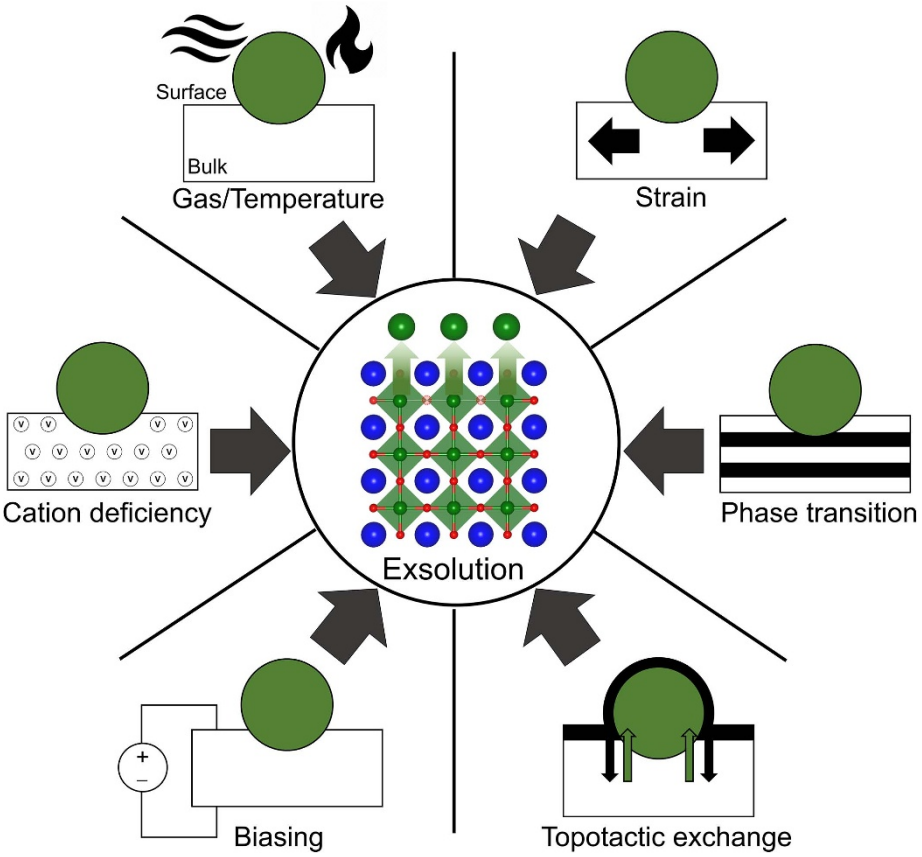

Figure 5. Driving forces to promote the exsolution in perovskite oxides: gas/temperature, cation deficiency, biasing, strain, phase transition, and topotactic exchange. In the driving forces, the green spheres indicate exsolved nanoparticle. In the middle circle, blue, green, and red spheres indicate A-site cation, B-site cation, and oxygen, respectively.

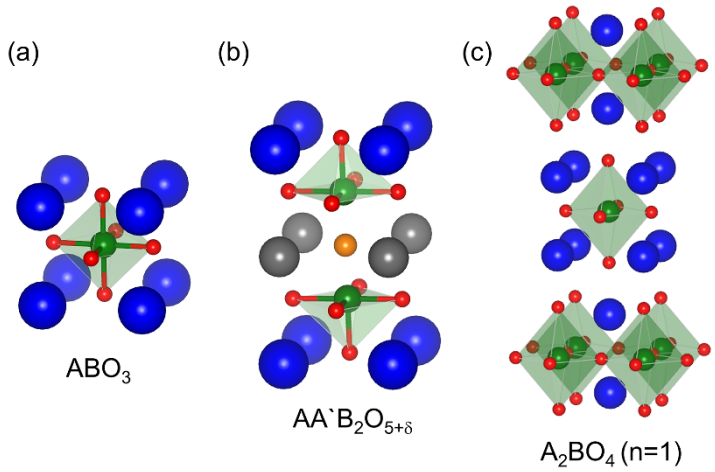

Figure 6. Crystal structures of (a) single perovskite (ABO_3), (b) double perovskite ($AA`B_2O_{5+\delta}$), and (c) RP perovskite ($A_{n+1}B_nO_{3\,n+1}$).

vicinity of the $LaFe_{1-x}Pd_xO_3$ surface. The $LaPdO_{3-y}$ layer on the surface allows Pd atoms to move in and out of the perovskite lattice without long-distance diffusion through the bulk during the redox cycles.

In the case of Pd exsolution, co-exsolution with Fe has been reported in B-site excessive stoichiometric $La_{0.8}Sr_{0.2}Fe_{0.9}Nb_{0.1}Pd_{0.04}O_{3-\delta}$ [18]. Fe^0 and Pd^0 metallic nanoparticles were confirmed to exsolve on the surface of the perovskite anode during operation under a hydrogen atmosphere. The introduction of Pd increased electrical conductivity and H_2-adsorption. In the study on exsolving Ru [19] from a host lattice, increasing the electrochemical kinetics of Ru had a more pronounced effect than increasing that of Ni. The exsolved Ru nanoclusters were smaller ($\leq$ 5 nm) than those of Ni (~10 nm), and there were more Ru

nanoclusters than Ni nanoclusters. An attempt was made to dope Ir on the B-site of $LaCrO_3$-based perovskite [21]. The CH_4 conversion of the dry reforming reaction reached 81% at 750 °C and was maintained for about 72 h without coke formation on the catalyst surface.

Among transition metals, early research on producing Ni nanoparticles was carried out based on $La_{1-x}Sr_xCr_{1-y}Ni_yO_{3-\delta}$ [22]. The catalytic properties improved with the formation of Ni nanoparticles under a reducing atmosphere, however, catalytic activity performance was not proportional to the amount of Ni. $La_{0.5}Sr_{0.5}Ti_{0.75}Ni_{0.25}O_{3-\delta}$ [23] containing a significant amount of Ni was also successfully synthesized and Ni nanoparticles were exsolved in a hydrogen atmosphere. As an anode of solid oxide fuel cell (SOFC), $La_{0.75}Sr_{0.25}Cr_{0.5}Mn_{0.3}Ni_{0.2}O_{2.8}$ [26] was studied and the limit of the solid solution of Ni was 20% in B site. The formation of Ni nanoparticles during the reduction process could facilitate the water steam dissociation. Gao *et al* [66] recently studied the energetics of Ni segregation in a $SrTiO_3$-based perovskite framework. They demonstrated that Ni preferentially segregates toward the (100)-oriented and $SrTiO_3$-terminated surfaces. The Ni surface segregation is energetically promoted by the presence of A-site and O-site vacancies, whereas the substitution of Sr^{2+} with La^{3+} hinders surface segregation. Sun *et al* reported on the production of coking-tolerant anodes by co-doping Ni and Ce [25]. Exsolved metallic Ni provides a strong active site for fuel oxidation reactions, while Ce species with redox couples provide abundant oxygen ions. Moreover, a SOFC equipped with a Ni/Ce co-doped lanthanum strontium titanate anode also showed good electrochemical performance and stability in both 5000 ppm H_2S/H_2 and dry CH_4.

Alloy nanocatalysts among transition metals have also been reported in stoichiometric perovskite. $La_{0.6}Sr_{0.4}Fe_{0.8}Ni_{0.2}O_{3-\delta}$ [27] showed excellent current density during CO_2 electrolysis and it was found that the material gained redox stability from the symmetry between reduction and re-oxidation (figure 7). In $(La_{0.75})(Sr_{0.25})(Cr_{0.5}Fe_{0.35}Ni_{0.15})O_3$ [28], it was demonstrated that the exsolution of bimetallic Fe-Ni alloy nanoparticles occurred on the surface of the perovskite. For strontium ferrites based perovskites, Liu *et al* [29] revealed that Fe-Ni nanoparticles can be exsolved from $Sr_2Fe_{1.4}Ni_{0.1}Mo_{0.5}O_{6-\delta}$ perovskite. They examined the redox reversibility of the exsolved Fe-Ni nanoparticles which were oxidized to transition metal oxides (Ni,Fe)O instead being reincorporated into the parent perovskite oxide at 800 °C in air. Fe-Cu alloy nanocatalysts were also exsolved in $SrFe_{0.8}Cu_{0.1}Nb_{0.1}O_{3-\delta}$ [67]. The high conductivity in 5% H_2/Ar was achieved because of the exsolved Fe (or Fe-Cu alloy). Co-Fe nanoparticles on $La_{0.3}Sr_{0.7}Cr_{0.3}Fe_{0.6}Co_{0.1}O_{3-\delta}$ [30] showed a redox process at 800 °C where the exsolved particles were completely reincorporated into the perovskite lattice.

2.2. Exsolution on non-stoichiometric single perovskite

For these stoichiometric compositions, most cations are present in the oxide matrix under a reducing atmosphere, which is not available for gas-phase catalysis. Additionally, the compositions undergo difficulties associated with phases involving undesirable A-site cations (equation (1)).

$$ABO_{3-\delta} \overset{\text{Exsolution}}{\rightarrow} (1-\alpha)\,ABO_{3-\delta''} + \alpha AO + \alpha B \tag{1}$$

$$A_{1-\alpha}BO_{3-\delta} \overset{\text{Exsolution}}{\rightarrow} (1-\alpha)\,ABO_{3-\delta'} + \alpha B \tag{2}$$

Therefore, A-site deficient perovskites (A/B < 1) have been proposed to alleviate these problems [8, 11, 68, 69]. In the systems, the exsolution reverts perovskite to a more stable 'defect-free' ABO_3 stoichiometry, thus inhibiting A-site segregation (equation (2)). Moreover, harder-to-reduce cations can also be exsolved and exsolution preferentially emerges on the surface [69]. For example, in A-site deficient $La_{0.4}Sr_{0.4}TiO_3$, extremely stable Ti cations can also be exsolved as TiO_2 on the surface of the perovskite [69]. Based on this finding, much research on A-site deficient perovskites has been conducted to create more metallic nanoparticles on stable supporting materials in the past few years. Neagu *et al* [8] systematically reported on the role of A-site deficiency in B-site exsolution. In an A-site stoichiometric sample, a smooth surface exhibits no exsolution, whereas nanoparticles are exsolved on the surface in the case of A-site deficient perovskite under reducing condition. When reducing A-site deficient perovskite $A_{1-\alpha}BO_{3-\delta}$, oxygen vacancies are introduced as oxygens are removed. The presence of oxygen vacancy can cause spontaneous the exsolution of B-site species, thus destabilizing the perovskite lattice and re-establishing the stoichiometry. The exsolved nanocatalyst is well anchored on the perovskite substrate and stable against agglomeration. Gao *et al* [15] reported Ni exsolution on a Sc-based A-site deficient perovskite material $La_{0.4}Sr_{0.4}Sc_{0.9}Ni_{0.1}O_{3-\delta}$. The reduced samples showed high electrochemical catalytic activity in symmetric-cell measurements with an area-specific resistance of 0.055 Ω cm^2 at 800 °C in a humid hydrogen atmosphere. For $LaMnO_3$ based perovskite, it has been reported that 20 mol% Ni-doped $LaMnO_3$, $La_{0.9}Mn_{0.8}Ni_{0.2}O_3$ [37] showed resistance to carbon fiber formation due to their strong interfacial bonding to the substrate. $La_{0.6}Sr_{0.3}Cr_{0.85}Ni_{0.15}O_{3-\delta}$

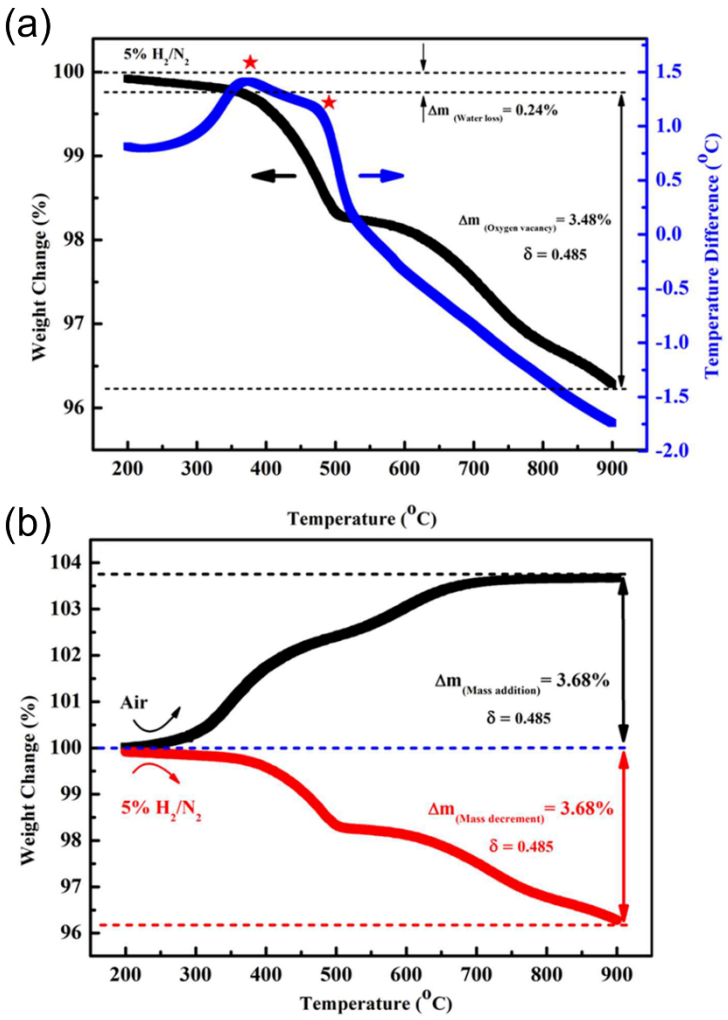

Figure 7. Thermogravimetric analysis testing. (a) Weight loss and differential thermal analysis of LSFN powders in 5% H_2/N_2 reducing atmosphere. (b) redox cycling ability test of LSFN powders, conducted first in a 5% H_2/N_2 reducing atmosphere in the ascending temperature range. After it was cooled, the analysis environment was switched to air flow in the same ascending temperature range. Reproduced with permission from [27] Copyright 2016, American Chemical Society.

[38] exhibited enhanced electrochemical performance and attractive redox stability in a 5000 ppm H_2S-H_2. A-site deficient perovskite also showed high performance in solid oxide electrolyzer cell (SOEC) cathodes [39]. Ni-anchored $La_{0.3}Sr_{0.7}TiO_{3-\delta}$ showed an approximately 20% better current efficiency than a bare cathode under an applied voltage of 2.0 V at 800 °C. For titanate co-doped with Mn and Ni, Ni metal can be exsolved to grow on the Mn-doped titanate [40]. This active catalyst showed the improved electrocatalytic activity and Faradaic efficiency for CO_2 electrolysis. Additionally, electrical conductivity is enhanced by the presence of metallic Ni. A great deal of research has been conducted recently on the exsolution for room temperature electrocatalysis. $La_{0.4}Sr_{0.4}Ti_{0.9}O_{3-\delta}$ [41] perovskites decorated with Ni nanoparticle have been reported to have catalytic activity in hydrogen evolution reaction (HER). This catalyst can work as a highly efficient HER electrocatalyst in basic media. As a bifunctional effect in the catalyst, the $La_{0.4}Sr_{0.4}Ti_{0.9}O_{3-\delta}$ perovskite promotes the dissociation of water and generation of hydrogen intermediates (H_{ads}), and the exsolved Ni nanoparticles facilitate the adsorption of hydrogen intermediates and generation of H_2. It was also possible to exsolve bimetallic nanoparticles such as Ni-Fe in A-site deficient perovskites. Sun *et al* [24] attempted to exsolve Ni-Fe bimetallic nanoparticles to improve the performance of a SOFC's monometallic anode, and they found that adding Fe helped to create more oxygen vacancies, and promoted the material reducibility. Zhu *et al* [46] revealed that A-site deficiency is important to avoid B-site deficiency after exsolution. In that study, the oxide phase in reduced $Sr_{0.95}Ti_{0.3}Fe_{0.63}Ni_{0.07}O_{3-\delta}$ showed a well-ordered perovskite structure, whereas the greater B-site deficiency in reduced $SrTi_{0.3}Fe_{0.63}Ni_{0.07}O_{3-\delta}$ resulted in a highly disordered and strained structure. Among transition metals other than Ni, Cu also can be exsolved. For example, $(La_{0.75}Sr_{0.25})_{0.9}(Cr_{0.5}Mn_{0.5})_{0.9}Cu_{0.1}O_{3-\delta}$ [42] can be used in CO_2 electrolysis by exsolving Cu on the surface of the perovskite. They observed that the current efficiencies of 85% were obtained with

Cu-decorated nanocatalysts for direct CO_2 electrolysis. Cu metal nanocatalysts were also effective in steam electrolysis [43]. The polarization resistance of $(La_{0.2}Sr_{0.8})_{0.9}Ti_{0.9}Cu_{0.1}O_{3-\delta}$ [43] was improved to 1.5 Ω cm^2 at 800 °C in hydrogen compared to 3 Ω cm^2 for the bare sample. In addition, the current efficiency of the Cu-anchored cathode is approximately 20% better than that of the bare cathode. Research on exsolution on Ag was carried out to develop SOFC cathode materials. Zhu *et al* reported that the exsolved $Sr_{0.95}Ag_{0.05}Nb_{0.1}Co_{0.9}O_{3-\delta}$ [44] electrode was very active for oxygen reduction reaction (ORR), achieving a very low area-specific resistance (~0.214 Ω cm^2 at 500 °C). In addition to high-temperature applications, Ag has excellent catalytic activity in other energy storage and conversion applications. An Ag nanoparticle modified $(La_{0.8}Sr_{0.2})_{0.95}MnO_{3-\delta}$ [45] was used as a cathode in dye-sensitized solar cells (DSSCs), displaying enhanced activity for the electrocatalytic triiodide (I_3^-) reduction reaction (IRR) in DSSCs as compared to the Ag/perovskite hybrids synthesized by physical mixing and impregnation methods.

In addition to the non-stoichiometric approach for exsolution, studies on other variables have been carried out to control B-site exsolution. These include altering factors such as lattice strain, electrical polarization, and gas environment. Strain effect plays an important role in determining the degree of exsolution. In this study of strain effect, a model system using epitaxial thin film is used. Tuning surface strain involves controlling the substrate, mechanism compression, and cation doping. A recent study using lattice strain [31] led to a high degree of nanoparticle exsolution. The epitaxial thin film was used to show the relationship between lattice strain and exsolved metal nanoparticles. This study indicated that the unidirectional lattice change in the strained thin film leads to a promotion of the nanoparticle nucleation with a large population density. Thus, lattice strain-enhanced exsolution in thin films can be controlled by adopting various lattice-mismatched substrates.

Another way to trigger exsolution is to apply a potential to the cell device [32–36]. Under reducing conditions for a SOEC cathode, several studies demonstrated that B-site dopants of A-site deficient perovskites can be exsolved to surface. It was confirmed for the first time that the Fe cation of $La_{0.4}Sr_{0.4}Fe_{0.06}Ti_{0.94}O_{2.97}$ [32] can also be exsolved. In a SOEC device with a $La_{0.43}Ca_{0.37}Ni_{0.06}Ti_{0.94}O_{3-\delta}$ [33] electrode, a finely dispersed array of anchored metal nanoparticles was grown in a few seconds at 900 °C, resulting in 2.75 A cm^{-2} at 1.3 V under an atmosphere of 50% water/N_2 gas, which is one of the highest performance of SOEC reported so far. The figure compares the characteristics when the sample is reduced by hydrogen versus a voltage-driven reduction, the latter of which was about two orders of magnitude faster than conventional reduction, and more nanocatalysts were produced. Some of the reported perovskite-based systems were used as the electrode for CO_2 electrolysis. Recently, $La_{0.43}Ca_{0.37}Ni_{0.06}Ti_{0.94}O_{3-\delta}$ and $La_{0.43}Ca_{0.37}Ni_{0.03}Fe_{0.03}Ti_{0.94}O_{3-\delta}$ perovskite electrodes were investigated to produce nanoparticles by exsolution under voltage in CO_2 atmosphere [34]. The cells with the reduced $La_{0.43}Ca_{0.37}Ni_{0.06}Ti_{0.94}O_{3-\delta}$ and $La_{0.43}Ca_{0.37}Ni_{0.03}Fe_{0.03}Ti_{0.94}O_{3-\delta}$ exhibited the current densities of 0.37 and 0.48 A cm^{-2} at 1.5 V in 100% CO_2, respectively. As reported by Ye *et al*, combining oxygen vacancies and exsolved catalytic nanoparticles produces an active interface for electrocatalytic CO_2 reduction [35]. Gan *et al* reported that *in situ* grown Ni nanoparticles on a $(La_{0.3}Sr_{0.7})_{0.9}Ti_{0.95}Ni_{0.05}O_{3-\delta}$ surface were enhanced by ~50% as compared to the bare a cathode for CO_2 electrolysis [36].

2.3. Exsolution on double perovskite

Because of its oxygen vacancy channel and structural characteristics, the double perovskite ($AA'B_2O_{5+\delta}$) exhibits excellent catalytic properties, such as fast surface oxygen exchange, rapid oxygen ion diffusion, and high electrical conductivity [70, 71]. As shown in figure 6(b), the A and A' sites are ordered along the *c*-axis, and oxygen vacancy is mainly formed in the A-site layer. In this regard, Sengodan *et al* reported $PrBaMn_2O_{5+\delta}$ (PBMO) layered oxygen-deficient double perovskite as ceramic anode for direct hydrocarbon SOFC [1]. The PBMO double perovskite was fabricated through a two-step sintering process. $Pr_{0.5}Ba_{0.5}MnO_{3-\delta}$ single perovskite with a mixture of cubic and hexagonal phases was synthesized in the air at 950 °C and then annealed in H_2 at 800 °C to fabricate the PBMO. The differential thermal analysis curve indicated an exothermic peak at approximately 400 °C in the reducing atmosphere, indicating that the phase transition from a single perovskite to a double perovskite occurred during the annealing process.

The phase transition under the reducing conditions leads to spontaneous exsolution without external control such as A-site defects. Additionally, the oxygen vacancy formation on the [PrO_x] layer also causes the exsolution of B-site transition metals [51]. Following the DFT using the Vienna *ab initio* simulations package (VASP) code, the double perovskite structure (−3.62 eV) has a much lower energy barrier for the exsolution of B-site atoms than a single perovskite (−4.82 eV). Therefore, the crystal reconstruction of perovskite is a favorable process for B-site cations exsolution. Indeed, MnO is known as having harder-to-reduce cations yet is also exsolved from $NdBaMn_2O_{5+\delta}$ double perovskite under reducing conditions [48].

Furthermore, Kwon *et al* reported the contribution of various transition metals toward exsolution on a $PrBaMn_{1.7}T_{0.3}O_{5+\delta}$ (T = Mn, Co, Ni, and Fe) double perovskite [47]. In their experimental results, Co, Ni,

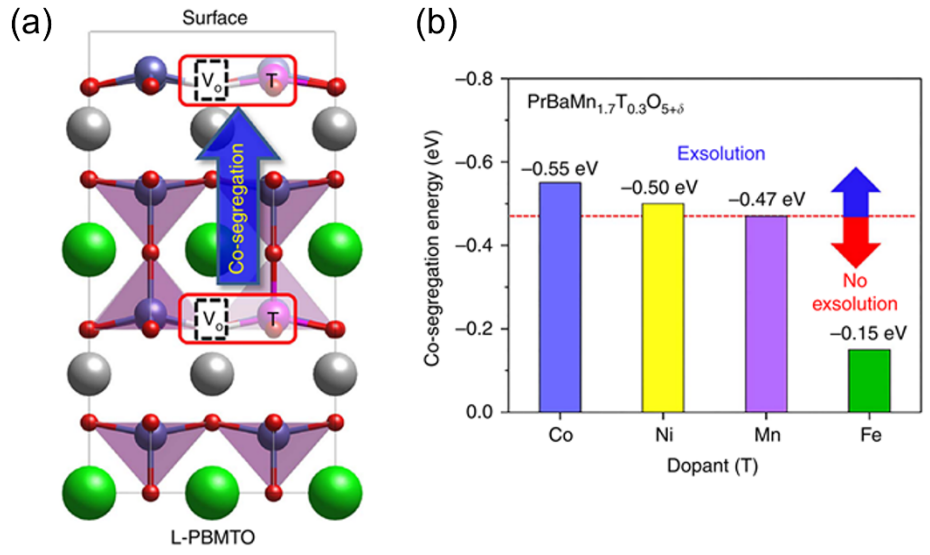

Figure 8. (a) Schematic image of co-segregation in the layered perovskite. Pr, Ba, Mn, T (Mn, Co, Ni, and Fe) and O atoms are shown as grey, green, dark blue, purple and red, respectively. The inset red boxes indicate the co-segregation of B-cation with an oxygen vacancy. (b) Comparison of the co-segregation energy with the dopant materials. (a) and (b) Reproduced with permission from [47] Copyright 2017, Nature Publishing Group.

and Mn were exsolved from the double perovskite, but Fe showed no exsolution. Transition metals generally have different degrees of reduction, however, the reducibility is not enough to explain the degrees of exsolution. Because the exsolution is a complex phenomenon that occurs from the inside of the lattice to the surface, the parent materials characteristics should be considered. The exsolution mechanism in the double perovskite is best described as the formation of a Schottky-type defect, which can be expressed as:

$$T_{Mn}^{X} + O_{O}^{X} \leftrightarrow TO + V_{O}^{oo} + V_{Mn}^{''} \tag{3}$$

where T_{Mn}^{X} is the B-site dopant in the Mn site with a zero net charge, O_{O}^{X} is oxygen in the oxygen site with a zero net charge, $V_{O}^{oo}$is the oxygen ion vacancy with a net charge of +2, and $V_{Mn}^{''}$represents the cation vacancy in the Mn site with a net charge of −2.

Therefore, the co-segregation energy of B-site transition metals with oxygen vacancies was introduced to verify the exsolution trends in the double perovskite. As shown in the schematic image (figure 8(a)), the B-site cations co-segregate with nearby oxygen toward the surface. Based on the Mn used as host cation, Co and Ni have higher co-segregation energy, and Fe has lower co-segregation energy, which is well supported by experimental results (figure 8(b)). Meanwhile, $PrBaMn_{1.7}Co_{0.3}O_{5+\delta}$ and $PrBaMn_{1.7}Ni_{0.3}O_{5+\delta}$ with exsolved metal nanoparticles show higher electrochemical performance than $PrBaMn_2O_{5+\delta}$ and $PrBaMn_{1.7}Fe_{0.3}O_{5+\delta}$ with exsolved oxide nanoparticles. This is because the exsolved metal nanoparticles have excellent catalytic activity for fuel oxidation [15, 72]. Additionally, no significant degradation was observed at a constant voltage of 0.6 V at 700 °C in C_3H_8 fuel, meaning that the double perovskite with exsolved metal nanoparticles has a high carbon coking tolerance in a hydrocarbon atmosphere.

Various catalyst design studies have been conducted based on the exsolution trends in the PBMO double perovskite. First, Co and Ni were co-doped on the Mn site of PBMO to investigate an alloy exsolution [49]. Since Co and Ni have higher co-segregation energies than Mn, both were expected to exsolve in the $PrBaMn_{1.7}Co_{0.1}Ni_{0.2}O_{5+\delta}$ (PBMCNO). As shown in the high-angle annular dark field (HAADF) image of PBMCNO with energy-dispersive x-ray spectroscopy elemental mapping images (figure 9(a)), Co and Ni coexist on the surface of PBMCNO, which indicates that Co-Ni alloy nanoparticles are exsolved after reduction at 850 °C in H_2. The lattice distance of the alloy nanoparticle is 0.127 nm (figure 9(d)), which is consistent with the lattice spacing of the (220) planes of the Co-Ni metal alloy.

It is reasonable to think that to form exsolved Co-Ni alloy nanoparticles, the aggregation of two doped B-site cations and the segregation to the surface should occur under a reducing atmosphere. Thus, two possible mechanisms, 'bulk alloy formation' and 'surface alloy formation', were considered to understand the alloy exsolution mechanism. During bulk alloy formation, Co–O_v (oxygen vacancy)–Ni aggregation occurs in the bulk of PBMCNO, after which Co–O_v–Ni segregates toward the surface. On the contrary, in the surface alloy formation, after Co–O_v–Co and Ni–O_v–Ni segregate to the surface, two metals with oxygen vacancy aggregate on the surface of PBMCNO. The Gibbs energies of aggregation in the bulk (bulk alloy

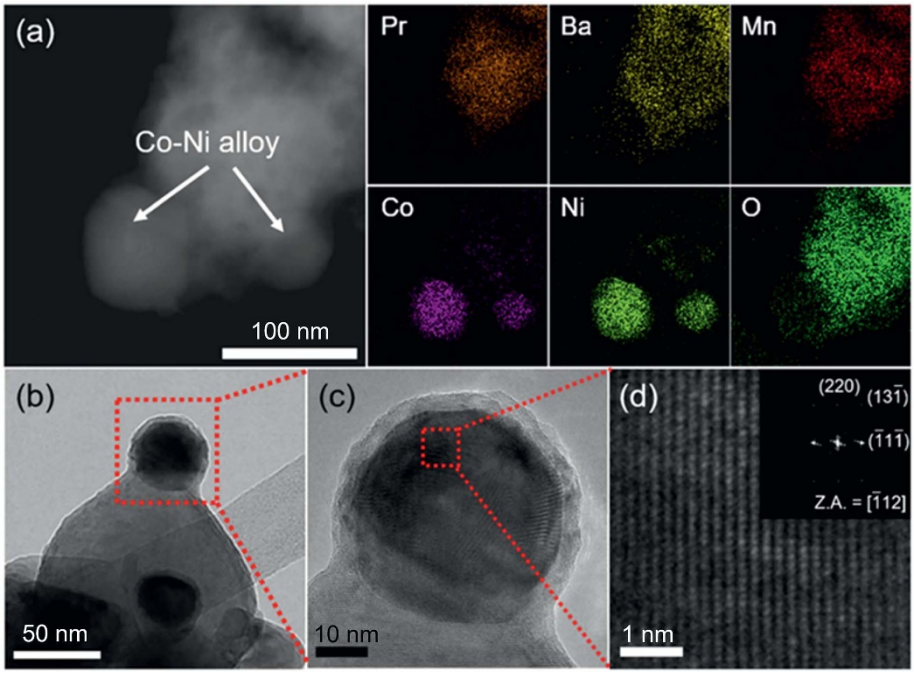

Figure 9. (a) High-angle annular dark-field (HADDF) image of PBMCNO with the EDS elemental map of Pr, Ba, Mn, Co, Ni, and O. (b) A bright-field (BF) TEM image and (c) the high-resolution (HR) TEM image of PBMCNO. (d) Magnified HR TEM image of exsolved Co-Ni alloy nanoparticles. (a), (b), (c), and (d) Reproduced with permission from [49] Copyright 2018, The Royal Society of Chemistry.

formation) and at the surface (surface alloy formation) are 0.02 eV and −0.01 eV, respectively, demonstrating that surface alloy formation is thermodynamically more favorable. The *in-situ* x-ray diffraction (XRD) results also confirmed that after the metallic Co located at 44.25° and the metallic Ni located at 44.7° were observed at 700 °C under an H_2 atmosphere, the two peaks combined to form a single peak at a temperature above 750 °C. To illustrate the notable improvement in the catalytic activity of the exsolved Co–Ni alloy, the dry reforming of methane was conducted at 800 °C–900 °C in a fixed-bed reactor. The CO_2 conversion of PBMCNO with Co–Ni alloy nanoparticles is almost four times higher than that of PBMO with MnO nanoparticles at 900 °C, which verifies that the exsolved Co-Ni metal alloy improves the catalytic activity for hydrocarbon oxidation.

In the general exsolution process, significant amounts of cations remain in the host bulk during the reduction process due to the limited diffusion rate of metal cations [62, 73]. In addition, the exsolution can cause structural instability because of excessive cation loss in the host material [74]. A recent study was conducted to increase the number of exsolved nanoparticles and stabilize the bulk using the exsolution trend and topotactic ion exchange [50]. The topotactic ion exchange is a solid-state reaction that reorganizes the cation locations [75, 76]. As mentioned previously, exsolution in stoichiometric double perovskite ($AA'B_{2-x}C_xO_{5+\delta}$) leaves B-site vacancies. In contrast, topotactic ion exchange maintains stoichiometric double perovskite without B-site vacancies after exsolution, which is illustrated by the following equation.

$$AA'B_{2-x}C_xO_{5+\delta} + xG \rightarrow AA'B_{2-x}G_xO_{5+\delta} + xC \quad (4)$$

where $AA'B_{2-x}C_xO_{5+\delta}$ represents the stoichiometric double perovskite, xG represents the quest cation, $AA'B_{2-x}G_xO_{5+\delta}$represents a new double perovskite without B-site vacancy, and xCrepresents the exsolved metal.

In the study of topotactic ion exchange, $PrBaMn_{1.7}Co_{0.3}O_{5+\delta}$ and Fe were selected as the host oxide and the guest cation, respectively. This is because Co (−0.55 eV) had higher co-segregation energy and Fe (−0.15 eV) had lower co-segregation energy than Mn (−0.47 eV) [47]. As a result of the topotactic ionic exchange between Co and Fe during the reduction process (figure 10), Fe entered the host material and Co exsolution occurred without B-site vacancies. To demonstrate the topotactic ion exchange process between host cation (i.e. Co and Mn) and guest cation (i.e. Fe), DFT calculation was conducted. The calculation of incorporation energy between B-site cations indicated that Co↔Fe (−0.41 eV) is thermodynamically more favorable than Mn↔Fe (0.22 eV). Therefore, as the amount of Fe guest cations increased, more Co cations were exsolved to the surface of the host material. The number of exsolved nanoparticles was thus verified to

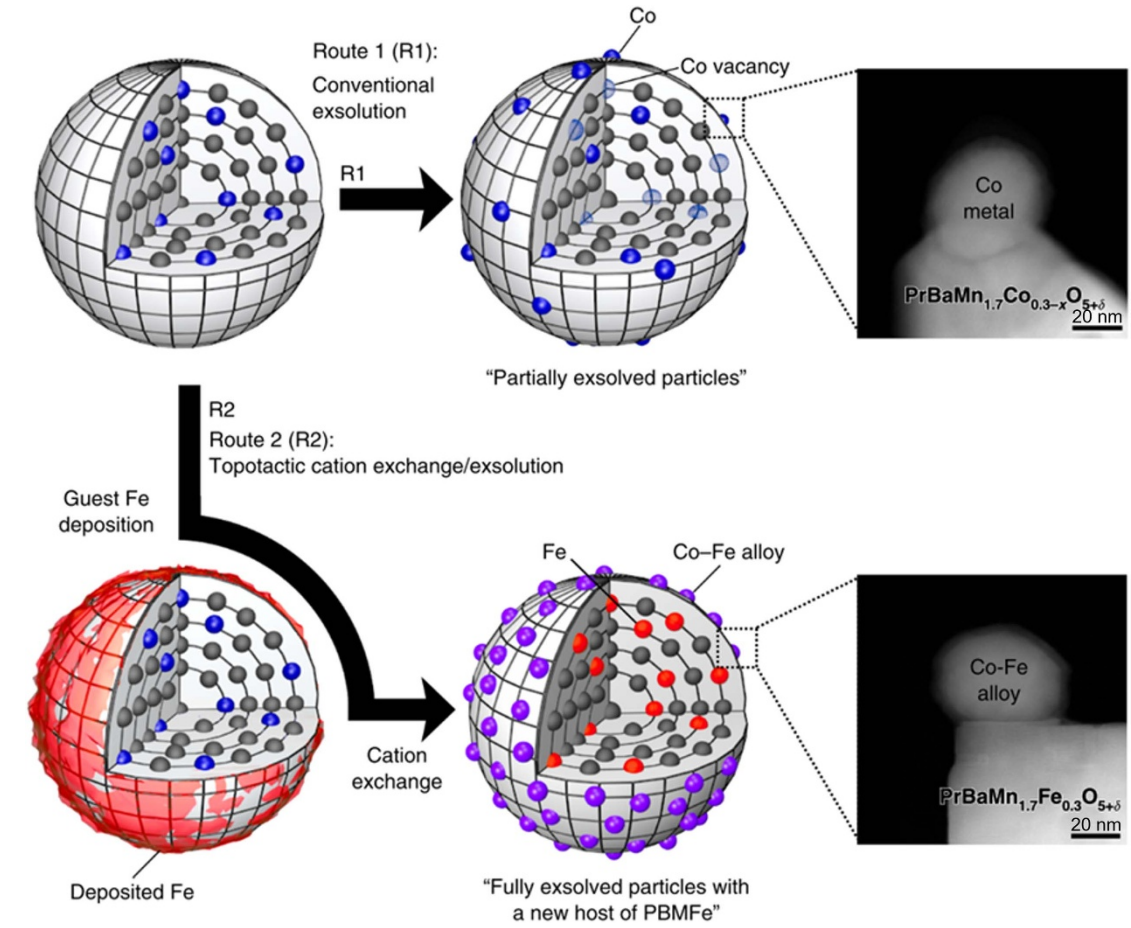

Figure 10. Schematic of exsolution process with and without topotactic ion exchange. Reproduced with permission from [50] Copyright 2019, Nature Publishing Group.

increase with the amount of guest Fe cations owing to the topotactic ion exchange, which greatly improved the electrochemical performance of the SOFC anode. The topotactic ion exchanged anode showed a maximum power density of 1.834 W cm^{-2} in humidified H_2, achieving the highest performance among the various recently developed SOFC anodes using exsolution [52, 77, 78].

2.4. Exsolution on Ruddlesden–Popper (RP) type perovskite

RP type perovskites have been widely researched as catalysts that can provide interesting physical and electrochemical properties because of their dimensionality effects and unique structure [79–82]. The RP structure consists of alternating perovskite and rock salt layers, which leads to fast ionic and electronic transport [83]. However, the conventional methods for fabricating RP perovskites require relatively high sintering temperatures ($\geq$ 1350 °C), which reduces specific surface area and catalytic activity. To decrease the sintering temperature, Yang *et al* utilized the phase transition of perovskite in a reducing atmosphere [52]. As a result of the reduction process, RP type perovskite $(Pr_{0.4}Sr_{0.6})_3(Fe_{0.85}Nb_{0.15})_2O_7$ with a Co-Fe alloy was formed from $Pr_{0.4}Sr_{0.6}Co_{0.2}Fe_{0.7}Nb_{0.1}O_{3-\delta}$ cubic perovskite. As with the double perovskite, exsolution occurs simultaneously with phase transition from the single perovskite to the RP type perovskite under the reduction process [54, 56, 84, 85].

Furthermore, Du *et al* reported the phase transition of perovskite with the exsolution in detail [53]. As shown in figure 11, the $Sr_2FeMo_{0.65}Ni_{0.35}O_{6-\delta}$ (SFMNi) perovskite is reduced to a $Sr_3FeMoO_{7-\delta}$ RP phase, a $SrFe_{1-y}Mo_yO_{3-\delta}$ cubic phase, and a Ni-Fe metallic alloy. The RP phase is a $Sr_3FeMoO_{7-\delta}$ layered perovskite ($A_3B_2O_7$), consisting of the two layers of $SrFe_{0.5}Mo_{0.5}O_{3-\delta}$ cubic perovskite (ABO_3) between the rock salt (AO) layers. The phase transition of the SFMNi can be expressed as:

$$Sr_2FeMo_{0.65}Ni_{0.35}O_{6-\delta} \rightarrow \frac{1}{2}SrFe_{0.7}Mo_{0.3}O_{3-\delta} + \frac{1}{2}Sr_3FeMoO_{7-\delta} + \frac{1}{8}Fe_{1.2}Ni_{2.8} + \frac{1}{2}O_2\,(g) \qquad (5)$$

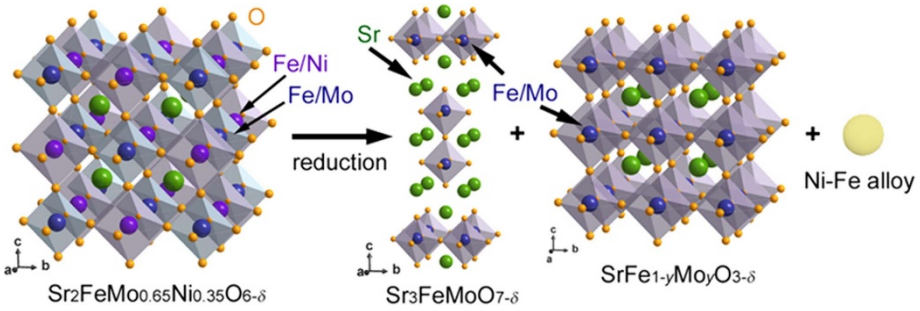

Figure 11. Schematic images for structural transformation of $Sr_2FeMo_{0.65}Ni_{0.35}O_{6-\delta}$ in reduction process. Reproduced with permission from [53], Copyright 2016 American Chemical Society.

Table 2. Characterization techniques for the study of exsolution.

Techniques	Depth resolutions	Description
Low-energy ion scattering (LEIS)	1–2 atomic layers	Elemental composition and lattice arrangement at the outmost layer
Auger electron spectroscopy (AES)	Several nanometers	Elemental composition of material surface
Scanning electron microscopy (SEM)	Several nanometers	Microstructure and morphology
X-ray photoelectron spectroscopy (XPS)	Several nanometers	Elemental composition and electronic state
Transmission electron microscopy (TEM)	Atomic-scale	Local elemental distribution with laterial resolution at the surface
Atomic force microscopy (AFM)	Several nanometers	Surface morphology

The transformed SFMNi anode with exsolved Ni-Fe alloy exhibited high catalytic activity toward the H_2 and CH_4 oxidation. In addition, a single-cell with an SFMNi anode showed no detectable degradation under a constant current density of 0.2 A cm^{-2} in CH_4, indicating good carbon coking tolerance of the ceramic anode.

The RP perovskites have excellent phase stability and reversibility under a redox cycle [55, 57–59]. Chung *et al* [55] reported that RP structure of $La_{1.2}Sr_{0.8}Mn_{0.4}Fe_{0.6}O_4$ (RPLSMF) and *in situ* B-site exsolution of Fe metal was obtained by *in situ* reduction of $La_{0.6}Sr_{0.4}Mn_{0.2}Fe_{0.8}O_3$ (LSMF) single perovskite. In the XRD results, the RPLSMF with Fe metal returned to the LSMF with no detectable secondary phase after re-oxidation in air. When the re-oxidized material was annealed again under the hydrogen atmosphere, the RPLSMF of the same composition as the first reduced sample was reconstituted, confirming the reversibility of phase transition during the redox cycle.

3. Characterization techniques of exsolution

The advanced characterization techniques are essential to identify the origin of exsolution and control its properties since exsolution occurs within a few nanometers. In recent years, the technological development of the analysis tool has been intensively improved, so in this part, a brief overview of the tool analyzing the exsolution is provided and summarized in table 2.

Low-energy ion scattering (LEIS) spectroscopy is a technique that can detect the composition and structure of the outmost surface. The observation range of LEIS reaches one or two atomic layers of the surface, which is one of the most precise surface analysis methods. Using the primary ion beam, the information on composition, element, and lattice arrangement can be obtained from the energy difference with the reflected primary ion beam. For example, Kilner's group studied surface chemistry of perovskite-based materials using LEIS [86]. They found that removal of the Sr-rich surface layer from $La_{0.6}Sr_{0.4}CoO_{3-\delta}$ could reduce the polarization resistance. Comprehensive studies have shown that LEIS appears to be a very useful characterization tool for analyzing the phenomenon of exsolution by providing profiling of elemental distribution in the near-surface regions of the perovskite oxides [86, 87].

Auger electron spectroscopy (AES) is a surface analysis technique that uses a high-energy electron beam to probe the composition of the material surface. This analysis technique collects information by detecting electrons emitted from higher energy levels called Auger electrons. Since this information includes the average of several atomic layers, exsolution information can be obtained in combination with depth profiling. Also, scanning electron microscopy (SEM) has been widely used to analyze surface morphology. This is one of the most intuitive devices to view particles after forming exsolved particles. Joo *et al* analyzed

by comparing the change in the number of exsolved particles of the SEM images to examine the correlation between the number of exsolved particles and electrochemical performance [50].

X-ray photoelectron spectroscopy (XPS) is a surface-sensitive quantitative spectroscopic technique that measures elemental composition, empirical formula, chemical state, and electronic state. The basic use is to obtain the oxidation state of B-site cation. Therefore, the metal nanoparticles exsolved on the surface and the cation state bound to oxygen in the bulk can be distinguished, thereby enabling quantitative analysis such as metal-cation ratio [88]. For example, it has been found that Ni is not present in the outermost atomic layer in the low-index (110) and (001) faces of a single crystal of $La_{1.67}Sr_{0.33}NiO_{4+\delta}$ through a combination of analytical techniques with LEIS and XPS [87]. Recently, research on surface chemistry has been conducted through *in situ* XPS. Shao-Horn's group analyzed the surface of $La_{1-x}Sr_xCoO_{3-\delta}$ thin film during heating and cooling cycles and found that the surface structure and chemistry are closely related to temperature [89].

Transmission electron microscopy (TEM) is an optical device where the electron beam passes through a specimen to create an image. Since the specimen is fixed on the grid and has a very thin thickness of 100 nm or less, electrons pass through interaction with the specimen. Energy-dispersive x-ray spectroscopy (EDS) is used for elemental and chemical analysis of samples. The combined use of TEM and EDS can provide information on local structures and compositions on surfaces, which can be very powerful tools for studying exsolution.

Atomic force microscopy (AFM) is a scanning probe microscope that uses the force between a probe and a sample surface atom. The surface image of the sample is formed by monitoring the change in the reflected laser caused by the tip bending as the tip scratches the surface. AFM does not require the conductivity of the sample nor the pretreatment of the sample which are required in SEM, therefore it can be used for analyzing various materials. Dragos *et al* have analyzed the dimension of exsolved particles by etching the sample surface [10].

4. Applications of exsolution

The exsolved nanoparticles on perovskite oxides have been intensively studied in the area of catalysis, electrocatalysis, and photocatalysis owing to their high catalytic properties and durability [39, 42, 50]. In particular, since the exsolution occurs in the reducing atmosphere at high temperatures, it has been widely used to design electrode materials in solid oxide cell (SOC) operated at 700 °C–850 °C [47, 49]. Exsolved metallic nanoparticles provide an excellent catalytic active site for fuel oxidation reaction in the SOC [47] and CH_4 conversion in the dry reforming reaction [50]. Besides, the exsolved composite oxides act as a superior catalyst for the HER, ORR, and oxygen evolution reaction (OER) [41, 90, 91]. Jiang *et al* reported that the improvement in electrochemical performance is mainly caused by the strong interaction and the electron transfer between the host perovskite oxide and exsolved metal nanoparticle [91]. In the photocatalysis, the exsolved metal nanoparticles are plasmonically active under visible light illumination, enhancing photocatalytic activity and the visible light absorption [92–94]. Excited free electrons within metal nanoparticles can be directly injected into the conduction band of perovskite oxide because of intimate contact between the metal and oxide, which participates in water reduction reactions to produce hydrogen [94].

5. Conclusion and outlook

Transition metal exsolution is a promising technique for designing catalysts in electrocatalysis and renewable energy. In the exsolution process, the metal cations exsolve from the parent oxide lattice to the oxide surface under a reducing atmosphere. Exsolved metal nanoparticles have high durability because of their unique feature of being socketed into the parent oxide surface. To understand the exsolution phenomena, parent oxide characteristics should be considered because the degree of exsolution is closely related to the oxide structure. Perovskite oxides (ABO_3) based materials have been mainly researched as the parent oxides for exsolution because of their excellent compositional structural flexibility. There are various structures in the perovskite oxides, each of which has a different main driving force for exsolution. In a single perovskite, harder-to-reduce cations can be exsolved by A-site deficiency of the perovskite, whereas in double and RP perovskites, phase transition under a reducing atmosphere spontaneously leads to exsolution without additional control. Those phenomena are demonstrated by advanced characterization techniques such as LEIS spectroscopy, AES, XPS, SEM, AFM, and TEM.

Until now, the exsolution phenomena in perovskite oxides have been widely studied, but there are still some fundamental open questions, such as how to maintain stable structure while the composition of the perovskite oxide changes from the stoichiometric to non-stoichiometric in the exsolution; what is the depth at which the exsolution occurs; how to achieve real time observation of the exsolution under operando

conditions (e.g. the SOC operating atmosphere). Therefore, in-depth understanding of exsolution and well-controlled experimental conditions with the advanced characterization techniques are required to unravel the scientific questions. These studies may provide significant insights into fundamental understanding of exsolution as well as the exploration of perovskite-based catalysts at various operating conditions of energy devices.

Acknowledgments

This work was supported by the Korea Institute of Energy Technology Evaluation and Planning (KETEP) and the Ministry of Trade, Industry & Energy (MOTIE) of the Republic of Korea (No. 20173020032120).

ORCID iD

Guntae Kim https://orcid.org/0000-0002-5167-0982

References

[1] Sengodan S, Choi S, Jun A, Shin T H, Ju Y-W, Jeong H Y, Shin J, Irvine J T S and Kim G 2015 Layered oxygen-deficient double perovskite as an efficient and stable anode for direct hydrocarbon solid oxide fuel cells *Nat. Mater.* **14** 205–9
[2] Awazu K, Fujimaki M, Rockstuhl C, Tominaga J, Murakami H, Ohki Y, Yoshida N and Watanabe T 2008 A plasmonic photocatalyst consisting of silver nanoparticles embedded in titanium dioxide *J. Am. Chem. Soc.* **130** 1676–80
[3] Kim S, Kwon O, Kim C, Gwon O, Jeong H Y, Kim K-H, Shin J and Kim G 2018 Strategy for enhancing interfacial effect of bifunctional electrocatalyst: infiltration of cobalt nanooxide on perovskite *Adv. Mater. Interfaces* **5** 1800123
[4] Cargnello M, Delgado Jaén J J, Hernández Garrido J C, Bakhmutsky K, Montini T, Calvino Gámez J J, Gorte R J and Fornasiero P 2012 Exceptional activity for methane combustion over modular Pd@CeO_2 subunits on functionalized Al_2O_3 *Science* **337** 713–7
[5] Schlupp M V F, Evans A, Martynczuk J and Prestat M 2013 Micro-solid oxide fuel cell membranes prepared by aerosol-assisted chemical vapor deposition *Adv. Energy. Mater.* **4** 1301383
[6] Gorte R J and Vohs J M 2009 Nanostructured anodes for solid oxide fuel cells *Curr. Opin. Colloid Interface Sci.* **14** 236–44
[7] Kim S, Jun A, Kwon O, Kim J, Yoo S, Jeong H Y, Shin J and Kim G 2015 Nanostructured double perovskite cathode with low sintering temperature for intermediate temperature solid oxide fuel cells *ChemSusChem* **8** 3153–8
[8] Neagu D, Tsekouras G, Miller D N, Ménard H and Irvine J T S 2013 *In situ* growth of nanoparticles through control of non-stoichiometry *Nat. Chem.* **5** 916–23
[9] Nishihata Y, Mizuki J, Akao T, Tanaka H, Uenishi M, Kimura M, Okamoto T and Hamada N 2002 Self-regeneration of a Pd-perovskite catalyst for automotive emissions control *Nature* **418** 164–7
[10] Neagu D, Oh T-S, Miller D N, Menard H, Bukhari S M, Gamble S R, Gorte R J, Vohs J M and Irvine J T S 2015 Nano-socketed nickel particles with enhanced coking resistance grown *in situ* by redox exsolution *Nat. Commun.* **6** 8120
[11] Oh T -S, Rahani E K, Neagu D, Irvine J T S, Shenoy V B, Gorte R J and Vohs J M 2015 Evidence and model for strain-driven release of metal nanocatalysts from perovskites during exsolution *J. Phys. Chem. Lett.* **6** 5106–10
[12] Li Y, Zhang W, Zheng Y, Chen J, Yu B, Chen Y and Liu M 2017 Controlling cation segregation in perovskite-based electrodes for high electro-catalytic activity and durability *Chem. Soc. Rev.* **46** 6345–78
[13] Hua B, Li M, Sun Y-F, Li J-H and Luo J-L 2017 Enhancing perovskite electrocatalysis of solid oxide cells through controlled exsolution of nanoparticles *ChemSusChem* **10** 3333–41
[14] Neagu D *et al* 2017 Demonstration of chemistry at a point through restructuring and catalytic activation at anchored nanoparticles *Nat. Commun.* **8** 1855
[15] Gao Y, Chen D, Saccoccio M, Lu Z and Ciucci F 2016 From material design to mechanism study: nanoscale Ni exsolution on a highly active A-site deficient anode material for solid oxide fuel cells *Nano Energy* **27** 499–508
[16] Neagu D *et al* 2019 *In situ* observation of nanoparticle exsolution mechanistic insight to nanostructure tailoring *ACS Nano* **13** 12996–3005
[17] Bierschenk D M, Potter-Nelson E, Hoel C, Liao Y, Marks L, Poeppelmeier K R and Barnett S A 2011 A highly efficient and Robust perovskite anode $O_{3-\delta}$–$Ce_{0.9}Gd_{0.1}O_{2-\delta}$ solid oxide fuel cell anodes exhibiting regenerative behavior *J. Power Sources* **196** 3089–94
[18] Li J, Wei B, Yue X and Zhe L 2018 A highly efficient and Robust perovskite anode with iron–palladium co-exsolutions for intermediate-temperature solid-oxide fuel cells *ChemSusChem* **11** 2593–603
[19] Kobsiriphat W, Madsen B D, Wang Y, Shah M, Marks L D and Barnett S A 2010 Nickel- and Ruthenium-doped lanthanum chromite anodes: effects of nanoscale metal precipitation on solid oxide fuel cell performance *J. Electrochem. Soc.* **157** B279–B284
[20] Madsen B D, Kobsiriphat W, Wang Y, Marks L D and Barnett S A 2007 Nucleation of nanometer-scale electrocatalyst particles in solid oxide fuel cell anodes *J. Power Sources* **166** 64–67
[21] Oh J H *et al* 2019 Importance of exsolution in transition-metal (Co, Rh, and Ir)-doped $LaCrO_3$ perovskite catalysts for boosting dry reforming of CH_4 using CO_2 for hydrogen production *Ind. Eng. Chem. Res.* **58** 6385–93
[22] Sauv,et A L and Irvine J T S 2004 Catalytic activity for steam methane reforming and physical characterisation of $La_{1-x}Sr_xCr_{1-y}Ni_yO_{3-\delta}$ *Solid State Ionics* **167** 1–8
[23] Arrivé C, Delahaye T, Joubert O and Gauthier G 2013 Exsolution of nickel nanoparticles at the surface of a conducting titanate as potential hydrogen electrode material for solid oxide electrochemical cells *J. Power Sources* **223** 341–8
[24] Sun Y-F, Li J-H, Cui L, Hua B, Cui S-H, Li J and Luo J-L 2015 A-site-deficiency facilitated in situ growth of bimetallic Ni–Fe nano-alloys: a novel coking-tolerant fuel cell anode catalyst *Nanoscale* **7** 11173–81
[25] Sun Y-F, Zhou X-W, Zeng Y, Amirkhiz B S, Wang M-N, Zhang L-Z, Hua B, Li J, Li J-H and Luo J-L 2015 An ingenious Ni/Ce co-doped titanate based perovskite as a coking-tolerant anode material for direct hydrocarbon solid oxide fuel cells *J. Mater. Chem.* A **3** 22830–8
[26] Jardiel T, Caldes M T, Moser F, Hamon J, Gauthier G and Joubert O 2010 New SOFC electrode materials: the Ni-substituted LSCM-based compounds $(La_{0.75}Sr_{0.25})(Cr_{0.5}Mn_{0.5-x}Ni_x)O_{3-\delta}$ and $(La_{0.75}Sr_{0.25})(Cr_{0.5-x}Ni_xMn_{0.5})O_{3-\delta}$ *Solid State Ionics* **181** 894–901

[27] Liu S, Liu Q and Luo J-L 2016 Highly stable and efficient catalyst with in situ exsolved Fe–Ni alloy nanospheres socketed on an oxygen deficient perovskite for direct CO $_2$ electrolysis *ACS Catal.* **6** 6219–28

[28] Papargyriou D, Miller D N and Irvine J T S 2019 Exsolution of Fe-Ni alloy nanoparticles from (La,Sr)(Cr,Fe,Ni)O_3 perovskites as potential oxygen transport membrane catalysts for methane reforming *J. Mater. Chem.* A **7** 15812–22

[29] Liu T *et al* 2020 Robust redox-reversible perovskite type steam electrolyser electrode decorated with in situ exsolved metallic nanoparticles *J. Mater. Chem.* A **8** 582–91

[30] Lai K-Y and Manthiram A 2018 Evolution of exsolved nanoparticles on a perovskite oxide surface during a redox process *Chem. Mater.* **30** 2838–47

[31] Han H, Park J, Nam S Y, Kim K J, Choi G M, Parkin S S P, Jang H M and Irvine J T S 2019 Lattice strain-enhanced exsolution of nanoparticles in thin films *Nat. Commun.* **10** 1471

[32] Tsekouras G, Neagu D and Irvine J T S 2013 Step-change in high temperature steam electrolysis performance of perovskite oxide cathodes with exsolution of B-site dopants *Energy Environ. Sci.* **6** 256–66

[33] Myung J, Neagu D, Miller D N and Irvine J T S 2016 Switching on electrocatalytic activity in solid oxide cells *Nature* **537** 528–31

[34] Chanthanumataporn M, Hui J, Yue X, Kakinuma K, Irvine J T S and Hanamura K 2019 Electrical reduction of perovskite electrodes for accelerating exsolution of nanoparticles *Electrochim. Acta* **306** 159–66

[35] Ye L, Zhang M, Huang P, Guo G, Hong M, Li C, Irvine J T S and Xie K 2017 Enhancing CO_2 electrolysis through synergistic control of non-stoichiometry and doping to tune cathode surface structures *Nat. Commun.* **8** 14785

[36] Gan L, Ye L, Tao S and Xie K 2016 Titanate cathodes with enhanced electrical properties achieved via growing surface Ni particles toward efficient carbon dioxide electrolysis *Phys. Chem. Chem. Phys.* **18** 3137–43

[37] Wei T, Jia L, Zheng H, Chi B, Pu J and Li J 2018 $LaMnO_3$-based perovskite with in-situ exsolved Ni nanoparticles: a highly active, performance stable and coking resistant catalyst for CO_2 dry reforming of CH_4 *Appl. Catal.* A **564** 199–207

[38] Sun Y, Li J, Zeng Y, Amirkhiz B S, Wang M, Behnamian Y and Luo J 2015 A-site deficient perovskite: the parent for *in situ* exsolution of highly active, regenerable nano-particles as SOFC anodes *J. Mater. Chem.* A **3** 11048–56

[39] Zhang J, Xie K, Gan Y, Wu G, Ding B, Zhang Y and Wu Y 2014 Composite titanate cathode enhanced with *in situ* grown nickel nanocatalyst for direct steam electrolysis *New J. Chem.* **38** 3434–42

[40] Li Y, Xie K, Chen S, Li H, Zhang Y and Wu Y 2015 Efficient carbon dioxide electrolysis based on perovskite cathode enhanced with nickel nanocatalyst *Electrochim. Acta* **153** 325–33

[41] Zhu Y, Dai J, Zhou W, Zhong Y, Wang H and Shao Z 2018 Synergistically enhanced hydrogen evolution electrocatalysis by in situ exsolution of metallic nanoparticles on perovskites *J. Mater. Chem.* A **6** 13582–7

[42] Li H, Sun G, Xie K, Qi W, Qin Q, Wei H, Chen S, Wang Y, Zhang Y and Wu Y 2014 Chromate cathode decorated with *in-situ* growth of copper nanocatalyst for high temperature carbon dioxide electrolysis *Int. J. Hydrog. Energy* **39** 20888–97

[43] Qi W, Ruan C, Wu G, Zhang Y, Wang Y, Xie K and Wu Y 2014 Reversibly *in-situ* anchoring copper nanocatalyst in perovskite titanate cathode for direct high-temperature steam electrolysis *Int. J. Hydrog. Energy* **39** 5485–96

[44] Zhu Y, Zhou W, Ran R, Chen Y, Shao Z and Liu M 2016 Promotion of oxygen reduction by exsolved silver nanoparticles on a perovskite scaffold for low-temperature solid oxide fuel cells *Nano Lett.* **16** 512–8

[45] Xu M, Wang W, Zhong Y, Xu X, Wang J, Zhou W and Shao Z 2019 Enhancing the triiodide reduction activity of a perovskite-based electrocatalyst for dye-sensitized solar cells through exsolved silver nanoparticles *J. Mater. Chem.* A **7** 17489–97

[46] Zhu T, Troiani H, Mogni L V, Santaya M, Han M and Barnett S A 2019 Exsolution and electrochemistry in perovskite solid oxide fuel cell anodes: role of stoichiometry in Sr(Ti,Fe,Ni)O_3 *J. Power Sources* **439** 227077

[47] Kwon O, Sengodan S, Kim K, Kim G, Jeong H Y, Shin J, Y -w J, Han J W and Kim G 2017 Exsolution trends and co-segregation aspects of self-grown catalyst nanoparticles in perovskites *Nat. Commun.* **8** 15967

[48] Sengodan S, Ju Y-W, Kwon O, Jun A, Jeong H Y, Ishihara T, Shin J and Kim G 2017 Self-decorated MnO nanoparticles on double perovskite solid oxide fuel cell anode by *in-situ* exsolution *ACS Sustainable Chem. Eng.* **5** 9207–13

[49] Kwon O, Kim K, Joo S, Jeong H Y, Shin J, Han J W, Sengodan S and Kim G 2018 Self-assembled alloy nanoparticles in layered double perovskite as a fuel oxidation catalyst for solid oxide fuel cells *J. Mater. Chem.* A **6** 15947–53

[50] Joo S, Kwon O, Kim K, Kim S, Kim H, Shin J, Jeong H Y, Sengodan S, Han J W and Kim G 2019 Cation-swapped homogeneous nanoparticles in perovskite oxides for high power density *Nat. Commun.* **10** 697

[51] Sun Y-F, Zhang Y-Q, Chen J, Li J-H, Zhu Y-T, Zeng Y-M, Amirkhiz B S, Li J, Hua B and Luo J-L 2016 New opportunity for *in situ* exsolution of metallic nanoparticles on perovskite parent *Nano Lett.* **16** 5303–9

[52] Yang C, Li J, Lin Y, Liu J, Chen F and Liu M 2015 *In situ* fabrication of CoFe alloy nanoparticles structured $(Pr_{0.4}Sr_{0.6})_3(Fe_{0.85}Nb_{0.15})_2O_7$ ceramic anode for direct hydrocarbon solid oxide fuel cells *Nano Energy* **11** 704–10

[53] Du Z, Zhao H, Yi S, Xia Q, Gong Y, Zhang Y, Cheng X, Li Y, Gu L and Świerczek K 2016 High-performance anode material $Sr_2FeMo_{0.65}Ni_{0.35}O_{6-\delta}$ with *in situ* exsolved nanoparticle catalyst *ACS Nano* **10** 8660–9

[54] Yang C, Yang Z, Jin C, Xiao G and Chen F 2012 Sulfur-tolerant redox-reversible anode material for direct hydrocarbon solid oxide fuel cells *Adv. Mater.* **24** 1439–43

[55] Chung Y S, Kim T, Shin T H, Yoon H, Park S, Sammes N M, Kim W B and Chung J S 2017 *In situ* preparation of a $La_{1.2}Sr_{0.8}Mn_{0.4}Fe_{0.6}O_4$ Ruddlesden-Popper phase with exsolved Fe nanoparticles as an anode for SOFCs *J. Mater. Chem.* A **5** 6437–46

[56] Sun K, Liu J, Feng J, Yuan H, He M, Xu C, Wang Z, Sun W and Qiao J 2017 Investigation of B-site doped perovskites $Sr_2Fe_{1.4}X_{0.1}Mo_{0.5}O_{6-\delta}$ (X=Bi, Al, Mg) as high-performance anodes for hybrid direct carbon fuel cell *J. Power Sources* **365** 109–16

[57] Zhou J, T -h S, Ni C, Chen G, Wu K, Cheng Y and Irvine J T S 2016 *In situ* growth of nanoparticles in layered perovskite $La_{0.8}Sr_{1.2}Fe_{0.9}Co_{0.1}O_{4-\delta}$ as an active and stable electrode for symmetrical solid oxide fuel cells *Chem. Mater.* **28** 2981–93

[58] Park S, Kim Y, Han H, Chung Y S, Yoon W, Choi J and Kim W B 2019 In situ exsolved Co nanoparticles on Ruddlesden-Popper material as highly active catalyst for CO_2 electrolysis to CO *Appl. Catal.* B **248** 147–56

[59] Kim K J, Rath M K, Kwak H H, Kim H J, Han J W, Hong S T and Lee K T 2019 A highly active and Redox-Stable $SrGdNi_{0.2}Mn_{0.8}O_{4\pm\delta}$ anode with in situ exsolution of nanocatalysts *ACS Catal.* **9** 1172–82

[60] Glazer A M 1975 Simple ways of determining perovskite structures *Acta Cryst.* A **31** 756

[61] Grabowska E 2016 Selected perovskite oxides: characterization, preparation and photocatalytic properties-A review *Appl. Catal.* B **186** 97–126

[62] Katz M B, Zhang S, Duan Y, Wang H, Fang M, Zhang K, Li B, Graham G W and Pan X 2012 Reversible precipitation/dissolution of precious-metal clusters in perovskite-based catalyst materials: bulk versus surface re-dispersion *J. Catal.* **293** 145–8

[63] Tanaka H, Uenishi M, Taniguchi M, Tan I, Narita K, Kimura M, Kaneko K, Nishihata Y and Mizuki J 2006 The intelligent catalyst having the self-regenerative function of Pd, Rh and Pt for automotive emissions control *Catal. Today* **117** 321–8

[64] Kobsiriphat W, Madsen B D, Wang Y, Marks L D and Barnett S A 2009 $La_{0.8}Sr_{0.2}Cr_{1-x}Ru_xO_{3-\delta}$-$Gd_{0.1}Ce_{0.9}O_{1.95}$ solid oxide fuel cell anodes: Ru precipitation and electrochemical performance *Solid State Ionics* **180** 257–64

[65] Hamada I, Uozumi A, Morikawa Y, Yanase A and Katayama-yoshida H 2011 A Density functional theory study of self-regenerating catalysts $LaFe_{1-x}M_xO_{3-y}$ (M = Pd, Rh, Pt) *J. Am. Chem. Soc.* **133** 18506–9

[66] Gao Y, Lu Z, You T L, Wang J, Xie L, He J and Ciucci F 2018 Energetics of nanoparticle exsolution from perovskite oxide *J. Phys. Chem. Lett.* **9** 3772–8

[67] Lan R, Cowin P I, Sengodan S and Tao S 2016 A perovskite oxide with high conductivities in both air and reducing atmosphere for use as electrode for solid oxide fuel cells *Sci. Rep.* **6** 31839

[68] Konysheva E Y, Xu X and Irvine J T S 2012 On the existence of A-site deficiency in perovskites and its relation to the electrochemical performance *Adv. Mater.* **24** 528–32

[69] Neagu D and Irvine J T S 2010 Structure and properties of $La_{0.4}Sr_{0.4}TiO_3$ ceramics for use as anode materials in solid oxide fuel cells *Chem. Mater.* **22** 5042–53

[70] Kim G, Wang S, Jacobson A J, Reimus L, Brodersen P and Mims C A 2007 Rapid oxygen ion diffusion and surface exchange kinetics in $PrBaCo_2O_{5+x}$ with a perovskite related structure and ordered A cations *J. Mater. Chem.* **17** 2500–5

[71] Choi S *et al* 2013 Highly efficient and robust cathode materials for low-temperature solid oxide fuel cells: $Prba_{0.5}Sr_{0.5}Co_{2-x}Fe_xO_{5+\delta}$ *Sci. Rep.* **3** 2426

[72] Cui S-H, Li J-H, Zhou X-W, Wang G-Y, Luo J-L, Chuang K T, Bai Y and Qiao L-J 2013 Cobalt doped $LaSrTiO_{3-\delta}$ as an anode catalyst: effect of Co nanoparticle precipitation on SOFCs operating on H_2S-containing hydrogen *J. Mater. Chem.* A **1** 9689–96

[73] Lin C, Jang J B, Zhang L, Stach E A and Gorte R J 2018 Improved coking resistance of "intelligent" Ni catalysts prepared by atomic layer deposition *ACS Catal.* **8** 7679–87

[74] Ma Q, Tietz F and Stöver D 2011 Nonstoichiometric Y-substituted $SrTiO_3$ materials as anodes for solid oxide fuel cells *Solid State Ionics* **192** 535–9

[75] Schöllhorn R 1980 Reversible topotactic redox reactions of solids by electron/ion transfer *Angew. Chem. Int. Ed. Engl.* **19** 983–1003

[76] Clearfield A 1988 Role of ion exchange in solid-state chemistry *Chem. Rev.* **88** 125–48

[77] Ding H, Tao Z, Liu S and Yang Y 2016 A redox-stable direct-methane solid oxide fuel cell (SOFC) with $Sr_2FeNb_{0.2}Mo_{0.8}O_{6-\delta}$ double perovskite as anode material *J. Power Sources* **327** 573–9

[78] Zhu T, Troiani H E, Mogni L V, Han M and Barnett S A 2018 Ni-substituted $Sr(Ti,Fe)O_3$ SOFC anodes: achieving high performance via metal alloy nanoparticle exsolution *Joule* **2** 478–96

[79] Amow G, Davidson I J and Skinner S J 2006 A comparative study of the Ruddlesden-Popper series, $La_{n+1}Ni_nO_{3n+1}$ (n = 1, 2 and 3), for solid-oxide fuel-cell cathode applications *Solid State Ionics* **177** 1205–10

[80] Kagomiya I, Jimbo K, Kakimoto K-I, Nakayama M and Masson O 2014 Oxygen vacancy formation and the ion migration mechanism in layered perovskite $(Sr,La)_3Fe_2O_{7-\delta}$ *Phys. Chem. Chem. Phys.* **16** 10875–82

[81] Du X, Zou G, Zhang Y and Wang X 2013 A novel strategy for low-temperature synthesis of Ruddlesden-Popper type layered perovskite $La_3Mn_2O_{7+\delta}$ for methane combustion *J. Mater. Chem. A* **1** 8411–16

[82] Fontaine M L, Laberty-Robert C, Ansart F and Tailhades P 2006 Composition and porosity graded $La_{2-x}NiO_{4+\delta}$ ($x \geq 0$) interlayers for SOFC: control of the microstructure via a sol-gel process *J. Power Sources* **156** 33–38

[83] Yoo S, Choi S, Shin J, Liu M and Kim G 2012 Electrical properties, thermodynamic behavior, and defect analysis of $La_n+1Ni_nO_{3n+1+\delta}$ infiltrated into YSZ scaffolds as cathodes for intermediate-temperature SOFCs *RSC Adv.* **2** 4648–55

[84] Liu M, Choi Y, Yang L, Blinn K, Qin W, Liu P and Liu M 2012 Direct octane fuel cells: a promising power for transportation *Nano Energy* **1** 448–55

[85] Wu N, Wang W, Zhong Y, Yang G, Qu J and Shao Z 2017 Nickel-iron alloy nanoparticle-decorated K_2NiF_4-type oxide as an efficient and sulfur-tolerant anode for solid oxide fuel cells *ChemElectroChem* **4** 2378–84

[86] Druce J, Téllez H, Burrie M, Sharp M D, Fawcett L J, Cook S N, McPhail D S, Ishihara T, Brongersma H H and Kilner A A 2014 Surface termination and subsurface restructuring of perovskite-based solid oxide electrode materials *Energy Environ. Sci.* **7** 3593–9

[87] Burriel M, Wilkins S, Hill J P, Muñoz-Márquez M A, Brongersma H H, Kilner J A, Ryan M P and Skinner S J 2014 Absence of Ni on the outer surface of Sr doped La_2NiO_4 single crystals *Energy Environ. Sci.* **7** 311–6

[88] Opitz A K, Nenning A, Rameshan C, Rameshan R, Blume R, Hävecker M, Knop-Gericke A, Rupprechter G, Fleig J and Klötzer B 2014 Enhancing electrochemical water-splitting kinetics by polarization-driven formation of near-surface iron(0): an in situ XPS study on perovskite-type electrodes *Angew. Chem. Int. Ed.* **54** 2628–32

[89] Feng Z, Crumlin E J, Hong W T, Lee D, Mutoro E, Biegalski M D, Zhou H, Bluhm H and Christen H M 2013 In situ studies of the temperature-dependent surface structure and chemistry of single-crystalline (001)-oriented $La_{0.8}Sr_{0.2}CoO_{3-\delta}$ perovskite thin films *J. Phys. Chem. Lett.* **4** 1512–8

[90] Lee J G, Myung J-H, Naden A B, Jeong O S, Shul Y G and Irvine J T S 2020 Replacement of Ca by Ni in a perovskite titanate to yield a novel perovskite exsolution architecture for oxygen-evolution reactions *Adv. Energy Mater.* **10** 1903693

[91] Jiang Y, Geng Z, Sun Y, Wang X, Huang K, Cong Y, Shi F, Wang Y, Zhang W and Feng S 2020 Highly efficient B-site exsolution assisted by Co doping in lanthanum ferrite toward high-performance electrocatalysts for oxygen evolution and oxygen reduction *ACS Sustainable Chem. Eng.* **8** 302–10

[92] Sun Y-F, Yang Y-L, Chen J, Li M, Zhang Y-Q, Li J-H, Hua B and Luo J-L 2018 Toward a rational photocatalyst design: a new formation strategy of co-catalyst/semiconductor heterostructures via in situ exsolution *Chem. Commun.* **54** 1505

[93] Xu X, Liu G and Azad A K 2015 Visible light photocatalysis by in situ growth of plasmonic Ag nanoparticles upon $AgTaO_3$ *Int. J. Hydrog. Energy* **40** 3672–8

[94] Yu J, Zhang L, Qian J, Zhu Z, Ni S and Liu G 2019 In situ exsolution of silver nanoparticles on $AgTaO_3$-$SrTiO_3$ solid solutions as efficient plasmonic photocatalysts for water splitting *Appl. Catal.* **256** 117818